Regional vulnerability and spreading of hyperphosphorylated tau in seeded mouse brain

Jan R. Detrez[a], Hervé Maurin[b], Kristof Van Kolen[b], Roland Willems[b], Julien Colombelli[c], Benoit Lechat[d], Bart Roucourt[e], Fred Van Leuven[f], Sarah Baatout[g,h], Peter Larsen[b], Rony Nuydens[b], Jean-Pierre Timmermans[a], Winnok H. De Vos[a,h,*]

[a] Laboratory of Cell Biology and Histology, Department of Veterinary Sciences, University of Antwerp, Universiteitsplein 1, 2610 Wilrijk, Belgium
[b] Department of Neuroscience, Janssen Research and Development, Turnhoutseweg 30, 2340 Beerse, Belgium
[c] Institute for Research in Biomedicine (IRB Barcelona), The Barcelona Institute of Science and Technology, 08028 Barcelona, Spain
[d] Laboratory for Experimental Mouse Genetics, Department of Human Genetics, Catholic University of Leuven, O&N1 Herestraat 49 bus 604, 3000 Leuven, Belgium
[e] reMYND NV, Gaston Geenslaan 1, Leuven, 3001, Belgium
[f] Lab Experimental Genetics, LEGTEGG, Dept. Human Genetics, KULeuven, O&N1 Herestraat 49 bus 602, 3000 Leuven, Belgium
[g] Belgian Nuclear Research Centre (SCK-CEN), Boeretang 200, 2400 Mol, Belgium
[h] Department of Molecular Biotechnology, Ghent University, Coupure Links 653, 9000 Ghent, Belgium

ARTICLE INFO

ABSTRACT

We have exploited whole brain microscopy to map the progressive deposition of hyperphosphorylated tau in intact, cleared mouse brain. We found that the three-dimensional spreading pattern of hyperphosphorylated tau in the brain of an aging Tau.P301L mouse model did not resemble that observed in AD patients. Injection of synthetic or patient-derived tau fibrils in the CA1 region resulted in a more faithful spreading pattern. Atlas-guided volumetric analysis showed a connectome-dependent spreading from the injection site and also revealed hyperphosphorylated tau deposits beyond the direct anatomical connections. In fibril-injected brains, we also detected a persistent subpopulation of rod-like and swollen microglia. Furthermore, we showed that the hyperphosphorylated tau load could be reduced by intracranial co-administration of, and to a lesser extent, by repeated systemic dosing with an antibody targeting the microtubule-binding domain of tau. Thus, the combination of targeted seeding and *in toto* staging of tau pathology allowed assessing regional vulnerability in a comprehensive manner, and holds potential as a preclinical drug validation tool.

1. Introduction

Alzheimer's disease (AD) is characterised by a progressive accumulation of amyloid beta peptides (Aß) and of tau protein in the brain (Masters et al., 2015). While both proteins are present in soluble form in physiologically conditions, increased concentrations of normal and aggregation-prone variants are observed in patients. Aggregation results in the formation of insoluble β-sheet–rich polymers, known as Aß fibrils and paired helical filaments (PHF), which further accumulate to amyloid plaques and neurofibrillary tangles (NFT), respectively. While amyloid plaque accumulation is one of the major hallmarks of AD, its presence does not correlate well with the extent of neurodegeneration, nor with the cognitive decline observed in patients (Brier et al., 2016). Moreover, roughly 30% of cognitively normal elderly show elevated levels of Aβ in the brain (Chételat et al., 2013). In contrast, accrual of abnormally hyperphosphorylated tau (further referred to as tau pathology) can be observed prior to the development of amyloid plaques, and correlates better with cognitive disease manifestations (Braak and Del Tredici, 2004; Cho et al., 2016; Spires-Jones and Hyman, 2014). Although subject of active debate, these findings suggests that tau pathology could be an important driver in AD aetiology.

While the triggers for the initial tau hyperphosphorylation and aggregation process remain elusive, tau pathology appears to follow a stereotypical spreading pattern in the affected brain (Brier et al., 2016). In AD patients, tau pathology starts in the locus coeruleus, and progresses to the transentorhinal region, the limbic areas, the temporal lobe and the insular cortex, to finally reach all other isocortical areas (Brettschneider et al., 2015). To better understand this process, efforts

have been made to mimic tau pathology in mice using inducible transgenes (De Calignon et al., 2012) or tau fibril seeding (Guo et al., 2016; Iba et al., 2013, 2015; Peeraer et al., 2015). As yet, work that focused on the spatiotemporal evolution of tau pathology has been performed on sectioned brain tissue. This approach is labour-intensive and time-consuming. Moreover, the destructive nature of sectioning leads to loss of material (thus reducing sensitivity) and complicates downstream standardisation and analytical procedures, such as brain atlas mapping (Barbier et al., 2017). Hence, there is a need for non-destructive methods that allow high-resolution imaging of the intact brain. With the advent of brain clearing and light-sheet microscopy, *in toto* imaging of the brain at cellular resolution has become feasible (Renier et al., 2016; Richardson and Lichtman, 2015). We have now optimized this technology for the visualisation and quantification of tau pathology in intact Tau.P301L mouse hemibrain. 3D atlas mapping and regional analysis revealed that stereotactic injection with synthetic or patient-derived tau fibrils induced a tau pathology pattern that resembled that of AD patients, and which was associated with a specific microglial subpopulation. By co-administration of a microtubule-binding domain targeting antibody, we also showed its potential for therapeutic intervention studies.

2. Materials and methods

2.1. Transgenic animals

Pathology progression was assessed in Tau.P301L (Terwel et al., 2005), Tau.P301S (Allen et al., 2002), 3xTG mice (Oddo et al., 2003) (Table S1). For injection studies, Tau.P301L were used at the age of 90 ± 5 days. All mice were maintained on a 12 h light/dark cycle, with food and water supplied *ad libitum* and with cage enrichment. Animals used in injection studies were single housed and randomised per treatment group, while non-injected animals were group housed. All experiments were performed in accordance with the principles of laboratory animal care and protocols approved under ECD files *2014–53, 2017–92* (University of Antwerp) and *628-Tau Spread* (Janssen Pharmaceutica). Reporting was done following the ARRIVE guidelines (Kilkenny et al., 2013).

2.2. Tau fibrils

A myc-tagged, truncated form of human P301L tau protein containing only the four microtubule-binding repeats (K18) was expressed in bacteria (Tebu-bio). K18 fragments (1 mg/ml) were incubated at 37 °C for 5 days in the presence of 133 μM heparin (MP Biomedicals). The mixture was centrifuged at 184.000 x g for 1 h, after which the pellet was resuspended in ammonium acetate buffer or PBS (Table S1) at 5 μg/μl (pH 7.0) and sonicated (Branson probe sonicator, amplitude 15%, total sonication time was 2 min in pulses of 2 s with 10 s interval). K18 fibrils were confirmed by native PAGE and by their potency to induce tau aggregation in cultured cells expressing Tau.P301L (Fig. S1A, B) (Holmes et al., 2014).

Enriched paired helical fragments (ePHFs) were purified from *post-mortem* brain tissue of a histopathologically confirmed AD patient (Greenberg and Davies, 1990). Typically, 5 g of tissue from the frontal cortex were homogenised in 10 volumes of cold buffer H (10 mM Tris, 800 mM NaCl, 1 mM EGTA, 10% sucrose, pH 7.4) using a glass/Teflon Potter tissue homogenizer (IKA Works, Inc.; Staufen, Germany) at 1.000 rpm. The homogenate was centrifuged at 27.000 *g* for 20 min and the supernatant was adjusted to a final concentration of 1% (*w/v*) N-lauroylsarcosine and 1% (*v/v*) 2-mercaptoethanol, and incubated for 2 h at 37 °C. The supernatant was centrifuged at 184.000 x g for 90 min at 20 °C, the pellet was washed with PBS and resuspended in 750 μl PBS, aliquoted and frozen at −80 °C.

2.3. Antibody treatment

PT83, the antibody targeting the microtubule binding domain of K18 ($_{267}$KHQPGG$_{277}$/$_{299}$HVPG$_{302}$/$_{329}$HHKPGG$_{334}$/$_{361}$THVPGG$_{366}$), was generated in mouse at Janssen Pharmaceutica (Vandermeeren et al., 2018). Binding of PT83 to K18 monomers and aggregates was confirmed (Fig. S1C). A mouse IgG (Centocor CNTO1037) was used as a control. Four treatment arms were defined: intracranial (i.c.) buffer (PBS) and intraperitoneal (i.p.) PBS, i.c. K18 with PT83 and i.p. PBS, i.c. K18 and i.p. PT83, and i.c. K18 with IgG and i.p. IgG. For i.c. administration, 0.5 μl PT83 (4 μg/ml) or 0.5 μl buffer was administered together with 1.5 μl tau fibrils (5 μg/ml), thus keeping a total injected volume of 2 μl. Repeated i.p. PT83 administration was done at 20 mg per kg bodyweight 4 times in the week preceding injection, followed by bi-weekly injections in the subsequent 3 weeks until sacrifice. All animals from this experiment were treated in parallel.

2.4. Stereotactic injection

Tau.P301L mice were deeply anaesthetised with isoflurane (2% in 36% oxygen) and fixed in a stereotactic frame (Neurostar). To correctly position the head, a tolerance was used in the dorsal-ventral (DV) axis with ΔDV(Bregma-Lambda) < 0.1 mm and ΔDV(ML Bregma $\pm$ 2) < 0.2 mm. Dipodolor (0.25 mg/kg; Janssen-Cilag) was administered *via* subcutaneous injection, and Xylocaine (AstraZeneca) was locally applied on the skull. A 30G syringe (Hamilton) was used for injecting 2 μl in the right hemisphere at a speed of 0.25 μl/min at the selected coordinates: anterior-posterior −1.83, medial-lateral +1.29 from Bregma, and dorsal-ventral +1.7 from the dura. Body weight was monitored before and weekly after injection, and no differences were observed between treatment and control groups for all injection experiments (not shown). Injection with 1.5 μl adeno associated virus (AAV) that expressed a free-floating green-fluorescent protein (GFP) under control of neuronal synapsin-1 promoter (pAAV-SEWB) was done with the same protocol to visualize the connectome of the injection site.

2.5. Clearing and fluorescent labelling

Animals were deeply anaesthetised by intraperitoneal injection (Nembutal, 150 mg/kg), following transcardial perfusion with heparinised PBS (Sigma H3393-50KU; 10 U/ml; 5 min) and 4% paraformaldehyde (Affymetrix USB. J19943; 5 min) at 2 ml/min. Brains were dissected, hemisected and post-fixed overnight in 4% PFA at 4 °C, followed by a PBS wash (3 × 15 min) and storage in PBS with 0.1% NaN$_3$ at 4 °C until further processing.

We optimized a microscopy approach to visualize tau pathology in cleared mouse hemibrain (Fig. S2). Validation of the clearing and labelling protocol is described in the supplemental methods and figures (Figs. S3, S4; Supplementary Movie S1). Fluorescent labelling and clearing of brain hemispheres were done based on the iDISCO+ protocol for all brains, except for GFP-labelled brains, which were cleared with uDISCO to preserve the GFP signal without additional post-hoc fluorescent labelling (Pan et al., 2016; Renier et al., 2016). Hyperphosphorylated tau was specifically detected using an AT8 antibody (pSer202/Thr205/PSer208, produced at Janssen Pharmaceutica). This antibody was labelled with a near-infrared fluorescent tag (PerkinElmer VivoTag 680XL) following the manufacturer's protocol prior to labelling (9.18 μg/ml in 1.8 ml for 7 days per hemisphere), yielding AT8-680XL. The conformation-sensitive optical probe pentameric formyl thiophene acetic acid (p-FTAA) was used for selective staining of protein aggregates (30 μM in 1.8 ml for 1 day per hemisphere) (Åslund et al., 2009). In case of microglial assessment, brains were mounted in a custom-made slicing tool for sectioning 4 mm thick coronal slices around the injection spot. Sections were rehydrated in a reversed methanol series, and incubated with an Iba1 antibody (Wako 019–19741) for 2 weeks, followed by a secondary Cy3-conjugated goat-anti-rabbit

antibody (Jackson 111–165-144) at 37 °C.

2.6. Light-sheet microscopy

Validation of the clearing and labelling performance (Fig. S3, Fig. S4) was done on a custom-built light-sheet microscope equipped with a AZ100M zoom body (Nikon) and an Orca R2 camera (Hamamatsu). Images were recorded at a total magnification of 1.32×, which corresponds to a pixel size of 4.92 μm. The z-step was 10 μm. Bidirectional excitation with a single light-sheet was achieved with 488 nm, 561 nm and 640 nm lasers. Emission was detected through bandpass filters (525/50 nm, 609/54 nm) and a far-red long-pass filter respectively (HQ BrightLine filters from AHF Analysentechnik).

All other cleared brain samples were acquired with an Ultramicroscope II (Lavision Biotec GmbH), equipped with an Olympus MVPLAPO 2× (NA 0.50) objective lens and DBE-corrected LV OM DCC20 dipping cap. Images were recorded with a Neo sCMOS camera (Andor) at a total magnification of 1.6× and a z-step of 10 μm resulting in $4 \mu m^2 \times 10 \mu m$ voxels. Images from the left and right light sheets were merged on the fly with a linear blending algorithm. A 488 nm, 561 nm and 640 nm laser with a 525/50 nm, 620/60 nm and 680/30 nm emission filter were used. Sagittal optical sections were recorded in a mosaic of two tiles. The exposure time was in the order of 150 ms, resulting in a recording time of ~ 30 min per hemisphere for three channels. Thick Iba1-stained sections were imaged as one 3D stack of coronal images.

2.7. Image analysis

To analyse AT8-positive, hyperphosphorylated tau deposition in a region-dependent manner, we developed an image analysis workflow allowing sequential image reconstruction, registration, segmentation and analysis, adapted from the Clearmap protocol (Renier et al., 2016) (Fig. S5A). First, images were stitched using the ImageJ *Grid/Collection Stitching* plugin (Preibisch et al., 2009). Next, the autofluorescence channel was downsampled to the atlas resolution (25 μm³) and aligned to a 3D autofluorescence reference brain atlas. To improve the registration accuracy, a population-based autofluorescence template was generated by averaging over 20 aligned hemispheres and subsequent mapping to the Allen Brain Atlas using *Elastix* (Kim et al., 2015; Klein et al., 2010) (Fig. S5B). The template was then aligned to the individual autofluorescence images, and the resulting transformation vector set was used for regional analysis of the AT8 signal. An inverse transformation was calculated for visualisation and reconstruction of the hemisected brains, which were visualised as horizontal and coronal maximum intensity projections (MIPs) or with 3D renders using Voreen (Meyer-Spradow et al., 2009). Images containing the AT8-680XL signals were pre-processed by applying a rolling ball background subtraction with a radius of 160 μm, and binarised with a user-defined, fixed threshold. A morphological opening operation was performed on the binary mask to remove small false-positive spots resulting from aspecific labelling, which are predominantly visible at the medial surface of the tissue. The autofluorescent channel was masked to delineate the contours of the sample, which were subsequently eroded using a minimum filter (radius 100 μm). This mask was used to remove spurious objects that are detected at the edge of the tissue resulting from aspecific labelling. Remaining larger non-specific objects in the AT8-680XL channel originating from blood vessels or from the surface of the brain tissue, were manually removed. Subsequently, the total number of AT8-positive voxels for a given hemibrain or brain region volume was calculated and expressed as a relative AT8 load (AT8 Load %). For every experiment, stacked bar graphs were drawn in which the AT8 load of individual brain regions was expressed as a fraction of the total hemibrain AT8 load, and where the AT8 load per condition was normalised to the maximum value (normalised AT8 load).

To visually represent the average AT8 load of one experimental

condition, the registered 3D images of individual hemibrains were averaged after growing AT8-positive voxels to 50 μm³ spheres. This growing step was necessary to overcome the loss of voxels after the down-sampling step that is required for registration. The resulting average 3D image was subsequently rendered using Voreen (Meyer-Spradow et al., 2009). To perform voxel-based analysis, AT8-positive voxels were represented as 375 μm³ spheres to generate heatmaps of the 3D AT8 distribution. Batch processing and validation tools, such as cross-sectional prints to assess the stitching, atlas registration and AT8 detection accuracy, were implemented to handle large sample groups.

To register the 4 mm coronal section to the atlas, a mask was used to limit the registration of the section to the corresponding region in the atlas template. Detection of Iba1 positive structures was done using the same pipeline, but with modified parameters for the consecutive image filters, *i.e.*, rolling-ball background subtraction (radius 400 μm), median filtering (radius 12 μm), and user-defined threshold. To avoid false-positive detection strongly labelled edges were manually removed. In correspondence with the calculation of AT8 load, the total number of Iba1-positive voxels for a given brain region was calculated and expressed as a fraction of the total hemibrain Iba1 load. The Iba1 load per condition was then normalised to the maximum value (normalised Iba1 load).

2.8. Statistics

Measurements were represented as means with standard error of means (SEM) in bar charts. Considering the limited number of biological replicates, non-parametric testing was performed. In non-injected Tau.P301L mice, a Kruskal-Wallis test with post-hoc Dunn tests was used to determine whether there was an increase in absolute AT8 load compared to the 6 M time point with a Holm–Bonferroni correction for multiple testing. For K18 and ePHF-injected mice, the Mann-Witney *U* test and Holm–Bonferroni correction was used to compare the AT8 load to buffer controls. For Iba1, the Mann-Witney U test and Holm–Bonferroni correction was used to compare the Iba1 load in injected *vs.* non-injected controls. To control for multiple comparisons across brain subregions, *p*-values were corrected to q-values with a false-discovery rate of 10% using the Benjamin-Hochberg procedure and significant q-values were indicated on the tile plot as dots (Benjamini and Hochberg, 1995). Considering the larger number of biological replicates in the PT83 experiment, analysis of variance (ANOVA) with post-hoc Dunnett's tests was performed using K18 + IgG (i.c.) as the control. A Shapiro-Wilks test confirmed that the data were normally distributed, and a Levene's test confirmed that the variance was not significantly different between treatment groups. Voxel-based analysis was performed for K18 samples with a p-value cut-off of 5%. Statistical differences were indicated when p-values whereby: $0.05 > p > 0.01$ (*), $0.01 > p > 0.001$ (**), and $p < 0.001$ (***).

3. Results

3.1. In toto microscopy reveals region-specific tau pathology in aging Tau.P301L mice

To benchmark the whole-brain microscopy approach, we quantified the evolution of tau pathology (measured as the number of AT8-positive voxels and therefore further referred to as AT8 load) in non-injected Tau.P301L mice between the age of 6 and 9 months. In line with earlier findings (Terwel et al., 2005), a progressive increase in the total AT8 load was observed with age in both brain hemispheres (Fig. 1A, B; Fig. S6A). At 6 months of age, AT8 positivity was limited to the brainstem, cortex and cerebellum, including the cerebellar granular cell layer (Fig. 1C). At the cellular level, AT8 signal was found in both the somatodendritic compartments of neurons as well as in the neuropil (Fig. 1C). By the age of 9 months, additional regions that initially had no detectable AT8 signal, such as the hypothalamus, cerebral nuclei and
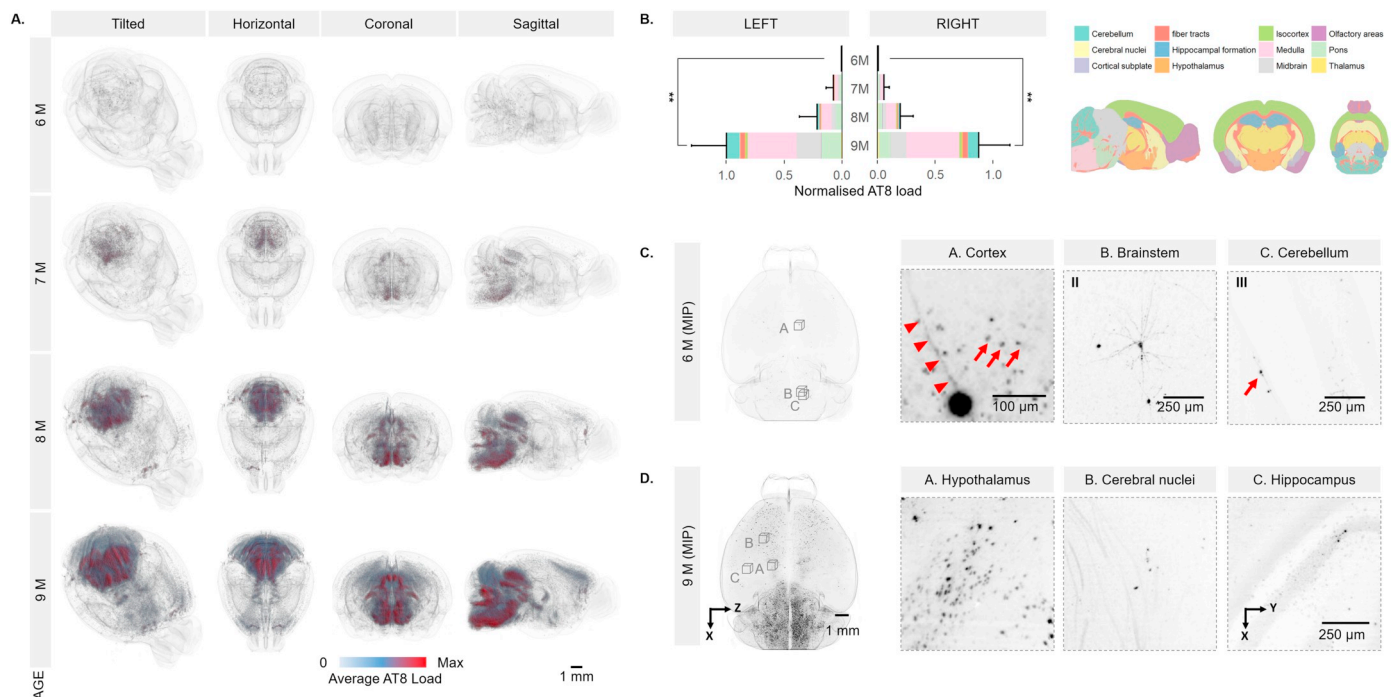
Fig. 1. Region-specific tau pathology in aging Tau.P301L mice. A. 3D rendered views of the average AT8 load in Tau.P301L mouse brain as a function of age; B. Regional analysis of AT8 load per age group. Bars show AT8 load (mean ± SEM) normalised to the maximum level (9 M, L); C. Atlas-transformed image of a 6-months-old Tau.P301L mouse brain with local maximum-intensity-projected insets showing staining in the neuronal soma, axons (red arrowheads) and the neuropil (red arrows) of cortical and brainstem neurons. AT8 staining is also present in the granular cell layer (red arrow) of the cerebellum; D. Atlas-transformed image of a 9-months-old Tau.P301L mouse with insets showing AT8 staining in the hypothalamus, cerebral nuclei and hippocampus. Number of biological replicates: 6 M (*n* = 3), 7 M (*n* = 2), 8 M (*n* = 6), and 9 M (n = 6). A representative set of biological replicates is shown in Fig. S6A.

hippocampus, displayed AT8 load as well (Fig. 1D). Thus, we conclude that *in toto* microscopy can be used to quantify tau pathology at the cellular level in a brain region-dependent manner and this at different stages of disease development.

3.2. K18 injection triggers AD-like tau pathology in Tau.P301L mice

With no AT8 signal in the forebrain, and a disproportionally large amount of AT8 signal in the cerebellum and brainstem, the staining pattern observed in Tau.P301L mice differs substantially from that of AD patients. Moreover, despite the progressive development of tau pathology in transgenic mice, it is impossible to determine whether it results from hyperphosphorylated tau spreading from the initial, more vulnerable sites, or rather from regional differences in cell-autonomous build-up of hyperphosphorylated tau. To directly interrogate the spatiotemporal spreading of hyperphosphorylated tau in a targeted manner, we therefore injected young (3 months) Tau.P301L mice with K18 fibrils in CA1 of the hippocampus (Peeraer et al., 2015). The choice for this time point was motivated by the desire to have a time window in which endogenous tau pathology would remain limited. Whereas buffer-injected, age-matched control mice displayed negligible amounts of AT8 load, a progressive increase in total AT8 load was observed in K18-injected animals over a period of 84 days post-injection (DPI) (Fig. 2A, B; Supplementary Movie S2). To confirm that the K18 injection induced multiple features of tau pathology – and not solely AT8 reactivity – we verified the presence of hyperphosphorylated tau in PHFs with an AT100 antibody, as well as the presence of protein aggregates using the ß-sheet selective oligothiophene dye p-FTAA, which binds both PHFs and NFTs (Åslund et al., 2009; Zheng-Fischhöfer et al., 1998) (Fig. S7). Of note, the AT8 staining pattern on sections (Fig. S7) was comparable to *in silico* generated slices (Fig. 2C), indicating that the clearing process did not dramatically affect the distribution of

hyperphosphorylated tau.

As early as 7 DPI, a significant increase in AT8 load was quantified in the hippocampus and isocortex of both ipsi- and contralateral side (Fig. 2B, C). A more resolved spatial analysis revealed that at this early time point, AT8 signal was also already present in distal regions such as the entorhinal area, auditory cortex, somatosensory cortex, and the thalamus (Fig. 2D; list of brain region abbreviations in Table S2). At 14 DPI, specific regions that were not yet affected at 7 DPI, including the hypothalamus, cerebral nuclei and the ipsilateral thalamus, were found positive for AT8. While the hippocampal AT8 load did not increase any further at the ipsilateral side at 21 DPI, all other contra- and ipsilateral regions continued to accumulate (AT8-positive) hyperphosphorylated tau up to 84 DPI. Of note, those regions (cerebellum, medulla, pons) that were found severely affected in older (8–9 months) non-injected Tau.P301L animals (Fig. 1), remained AT8-negative up to 84 DPI.

CA1 becomes affected at Braak stage II in AD (Braak and Braak, 1991). To find out to what extent tau pathology development would differ upon targeting a region that becomes affected at an even earlier stage, we also injected K18 in the afferent entorhinal area (ENT), a Braak stage I region (Fig. S8). Despite similarities in the spreading pattern, we observed injection site-specific differences. For example, the claustrum (CLA) and endopiriform nucleus (EP) were more affected upon ENT injection, whereas the contralateral cornu ammonis (CA) and thalamus (TH) were specifically more affected upon CA1 injection. Yet, despite these quantitative differences, the typical regions that become affected in AD patients (*e.g.* rhinal area, hippocampus, subiculum, thalamus and cortical association area's) were found AT8-positive in both conditions. This indicates that targeted seeding in early Braak stage regions induces a spatiotemporal spreading pattern of hyperphosphorylated tau that resembles more closely that observed in human AD patients, when compared to non-injected, aged Tau.P301L mice.
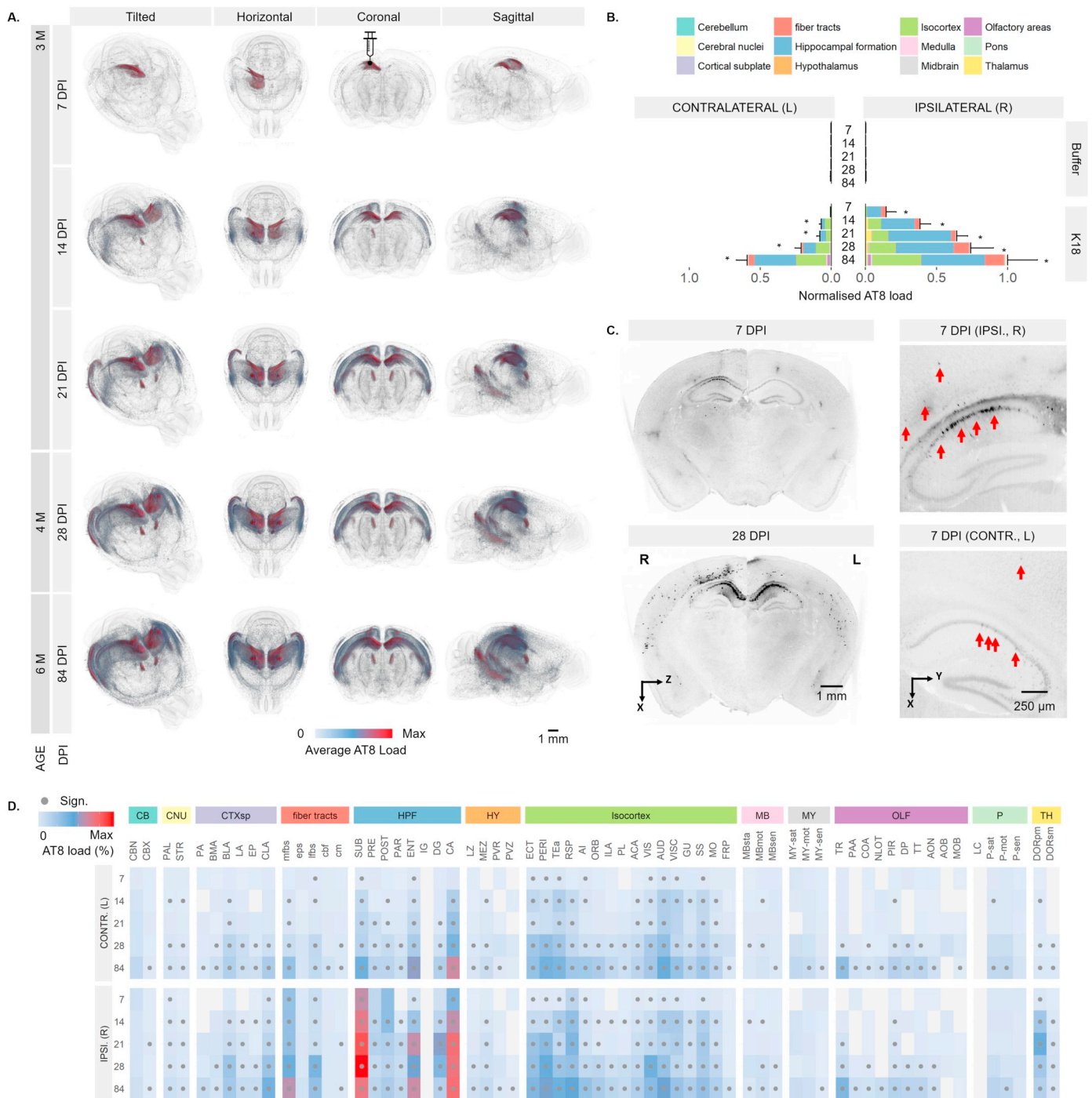
Fig. 2. K18-induced tau pathology in Tau.P301L mice. A. 3D rendered views of the average AT8 load in K18-injected Tau.P301L mouse brains as a function of injection time (DPI); B. Regional analysis of AT8 load over time. Bars show AT8 load (mean ± SEM), normalised to the maximum load (9 M, R); C. Atlas-transformed data shown with an inverted look-up-table. Insets show the AT8 positive staining in the ipsi- and contralateral hippocampus and cortex (red arrows) on the raw images; D. Tile plot showing detailed spatiotemporal fingerprint of AT8 load in K18-injected animals. The values were square root transformed to compress the dynamic range. Dots represent regions that are significantly different from age-matched buffer controls after FDR correction. A representative set of biological replicates is shown in Fig. S6B, staining for other tau pathology markers are shown in Fig. S7, and brain abbreviations are listed in Table S2. The number of biological replicates is $n \geq 4$ (Table S1).

3.3. K18 injection induces a specific microglial response

Increasing evidence suggests that microglia contribute to the progression of tau pathology (Perea et al., 2018). Hence, we evaluated the microglial response to K18 injection. To this end, an additional experiment was performed in which a mouse cohort was investigated at 25, 74 and 119 DPI to observe both early and chronic microgliosis on induced tau pathology. Hemispheres were first labelled with AT8 and subsequently trimmed to 4 mm blocks surrounding the injection site and rehydrated for microglial labelling with an Iba1 antibody (Fig. 3A). Although the injection itself triggered strong microgliosis (as detected by Iba1 reactivity) along the injection tract in both K18-injected animals and buffer controls, a significantly stronger Iba1 load was found in the ipsilateral hemisphere of K18-injected mice at 25 DPI. The
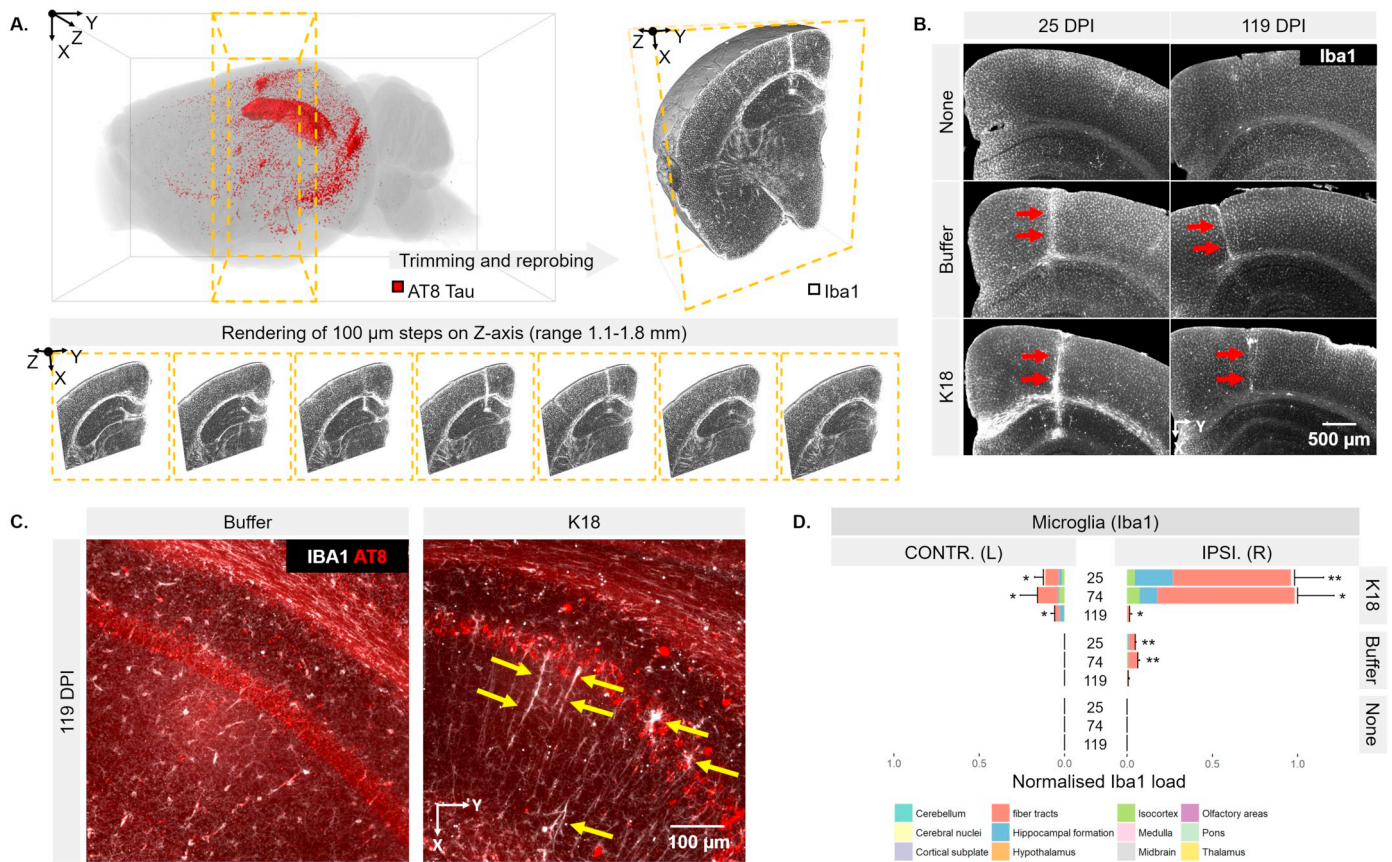
Fig. 3. K18 injection induces a microglial response. A. The left panel shows a 3D rendering of AT8 labelled hemispherere, which was subsequently trimmed (yellow lines) to a 3 mm thick section and labelled for Iba1 (Fig. S2C). The right panel shows a 3D rendering of the Iba1 staining, with insets highlighting the microglial response surrounding the injection site represented as consecutive 100 μm virtual sections; B. Representative images of treatment groups shows increased Iba1 staining round the injection tract (red arrows), corpus callosum and hippocampus; C. At 119 DPI, Iba1-positive microglia are in the vicinity of AT8-postive neurons of the hippocampus, and display a rod-like phenotype and swollen cell bodies (yellow arrows); D. Quantification shows a transient accumulation of Iba1-positive cells, most prominently in the corpus callosum, which largely disappears at 119 DPI. Bars show normalised Iba1 load (mean ± SEM). The number of biological replicates is $n \geq 4$ (Table S1).

accumulation of Iba1-positive cells around the injection tract, the corpus callosum and hippocampal formation, was still present at 74 DPI, but decreased significantly at 119 DPI (Fig. 3B, C). In contrast, AT8 load increased from 25 DPI to 74 DPI and remained high at 119 DPI (Fig. S9). This indicates that the microglial recruitment was not solely determined by the presence of hyperphosphorylated tau deposits. Intriguingly, we observed a subpopulation of microglia with swollen cell body and/or rod-like phenotype in K18-injected animals (Fig. S10A). This subpopulation was observed to a far lesser extent in buffer and non-injected controls and persisted up to 119 DPI. While the unusually large soma of these cells often resided in the vicinity of AT8-positive neurons, they did not colocalise *per se* (Fig. S10B). TMEM119 staining confirmed the microglial nature of these cells, whereas positivity for CD11B and F4/80-positive suggested they represent a subtype of reactive microglia (Fig. S10C). While the injection also promoted astrogliosis around the injection tract (as detected by increased GFAP reactivity), we did not observe changes in astrocyte abundance at the contralateral side between treatment groups at 119 DPI (Fig. S10D). Thus, we conclude that K18 injection triggers a transient accumulation of Iba1-positive microglia that extends up to 70 DPI, especially around the injection tract, but also recruits rod-like and swollen microglia which persist at least up to 119 DPI.

3.4. K18-induced tau pathology follows anatomical connections

Although the AT8 load developed in and proximal to the injection site, distally connected brain regions, including the ipsilateral

entorhinal area, hypothalamic regions and the contralateral brain regions were affected as well (Fig. 4A). Conversely, some proximal sites, such as the ipsilateral dentate gyrus, were only affected at 14 DPI (Fig. 2D). This indicates that regional accrual of hyperphosphorylated tau is not solely determined by the distance to the injection site. To investigate whether this differential vulnerability was determined by anatomical connections in the brain, we compared the observed AT8 distribution after K18 injection with GFP patterns obtained by injecting a pAAV-SEWB vector at the exact same coordinates in CA1 (Fig. 4A, B). At 21 DPI, there was a high correlation between both markers (Pearson correlation 0.69; Fig. 4C). Distal regions that showed high AT8 load, such as the entorhinal area and hypothalamus, also showed high GFP levels, while a proximal region such as the ipsilateral dentate gyrus was low for both markers (Fig. 4C). This shows that many of the affected regions represent anatomical projections from or to the CA1 injection site. Furthermore, AT8 staining was observed in both afferent (*e.g.,* dentate gyrus, CA3) and efferent regions (*e.g.,* subiculum, entorhinal area). Since the AT8 antibody does not recognize K18 fibrils (Malia et al., 2016), this observation points to anterograde and retrograde spreading of hyperphosphorylated tau. A notable exception was the absence of AT8 and GFP signal in the locus coeruleus. Importantly, tau pathology was also evident in regions that do not have direct projections from or to CA1 as evidenced by lack of GFP signal (the cortical subplate, pons, and specific subregions of the olfactory areas and cortical regions) (Fig. 4C). This suggests that spreading of hyperphosphorylated tau not only occurs within anatomical projections from the injection site, but might also be transmitted to secondary regions.
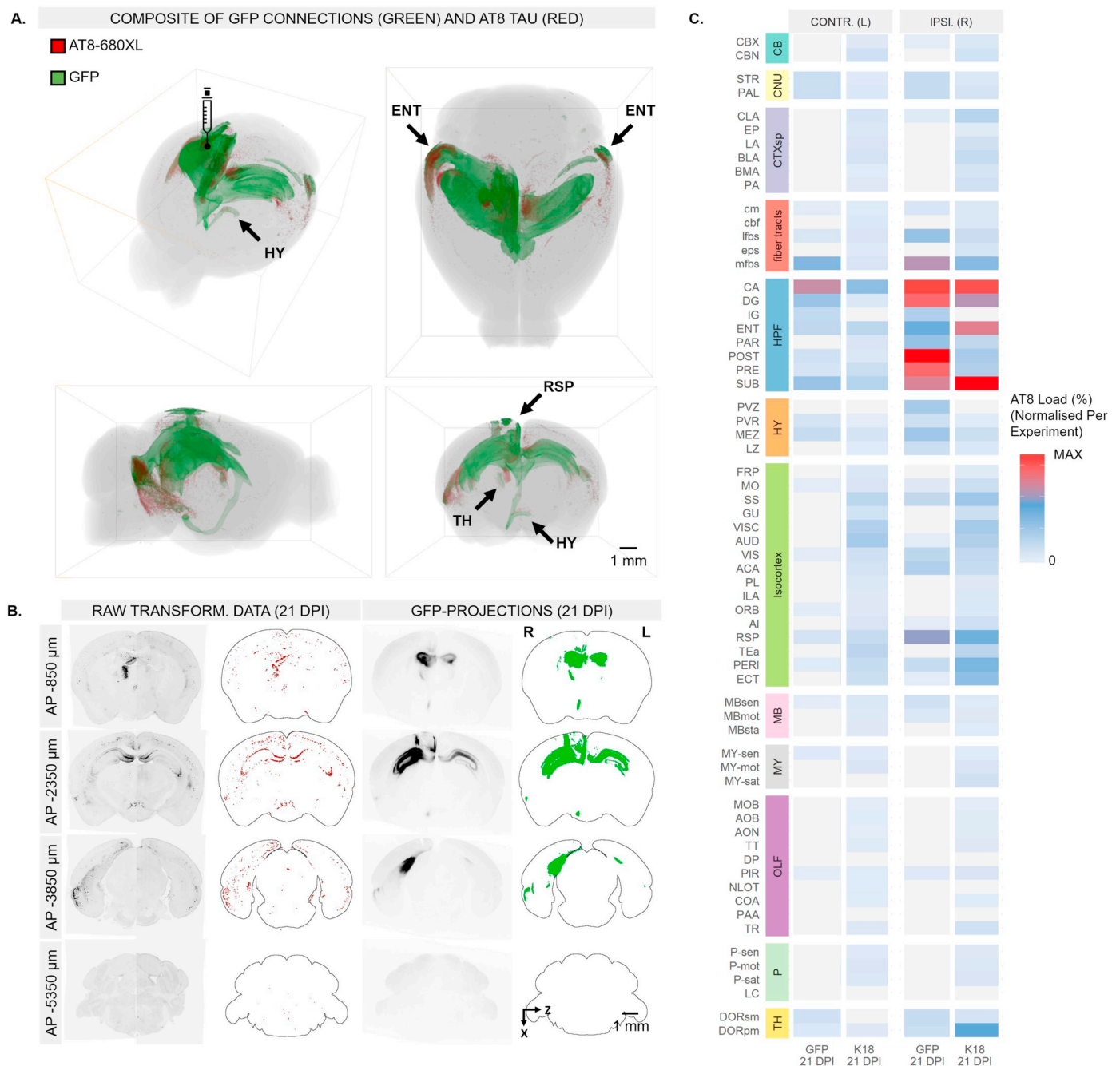
Fig. 4. K18-induced tau pathology follows anatomical connections. A. Composite 3D rendering of the GFP connections after uDISCO clearing and AT8 load from a representative iDISCO + cleared brain at 28 DPI. Anatomical connections of the injections site are indicated, including the thalamus (TH), hypothalamus (HY), ispi- and contralateral entorhinal area (ENT) and the retrosplenial area (RSP); B. The first two columns represent atlas-transformed AT8 virtual slices and segmented voxels for a 21 DPI K18-injected mouse brain. Virtual slices and segmented voxels of the corresponding GFP data are show in the last two columns; C. Tile plots of AT8 load after K18 injection at 84 DPI compared to the GFP projection map generated after uDISCO clearing. The regional AT8 load was square root transformed to compress the dynamic range. The number of biological replicates is 2.

3.5. Injection with ePHFs induces similar spreading patterns as K18 injection

While synthetic K18 fibrils display strong seeding capability in Tau.P301L mice, they may do so in a way that is different from pathological tau fibrils that naturally develop in the brain of AD patients. Hence, similar injection experiments were performed with enriched paired helical fragments (ePHFs) purified from AD brain (Guo et al., 2016), using extracts from healthy individuals as a control (Fig. 5A, B). At 28 DPI, minute AT8-positive staining was observed in the axonal tracts of the alveus of the ipsi- and contralateral hippocampus; this, in stark contrast with the strong somatic staining observed at the same timepoint after K18 injection (Fig. 5C). At 84 DPI, however, a significant increase in total AT8 load was evident, with strong AT8 accrual in the hippocampal formation, the cortex and the fibre tracts of both hemispheres (Fig. 5C). Regional analysis of the AT8 load revealed a strong resemblance with that of the K18-injected mice at 84 DPI (Pearson correlation 0.75; Fig. 5D). A notable difference with K18-incoluated brain was the virtual absence of AT8 load in contralateral olfactory area and cortical subplate. Thus, although the affected regions
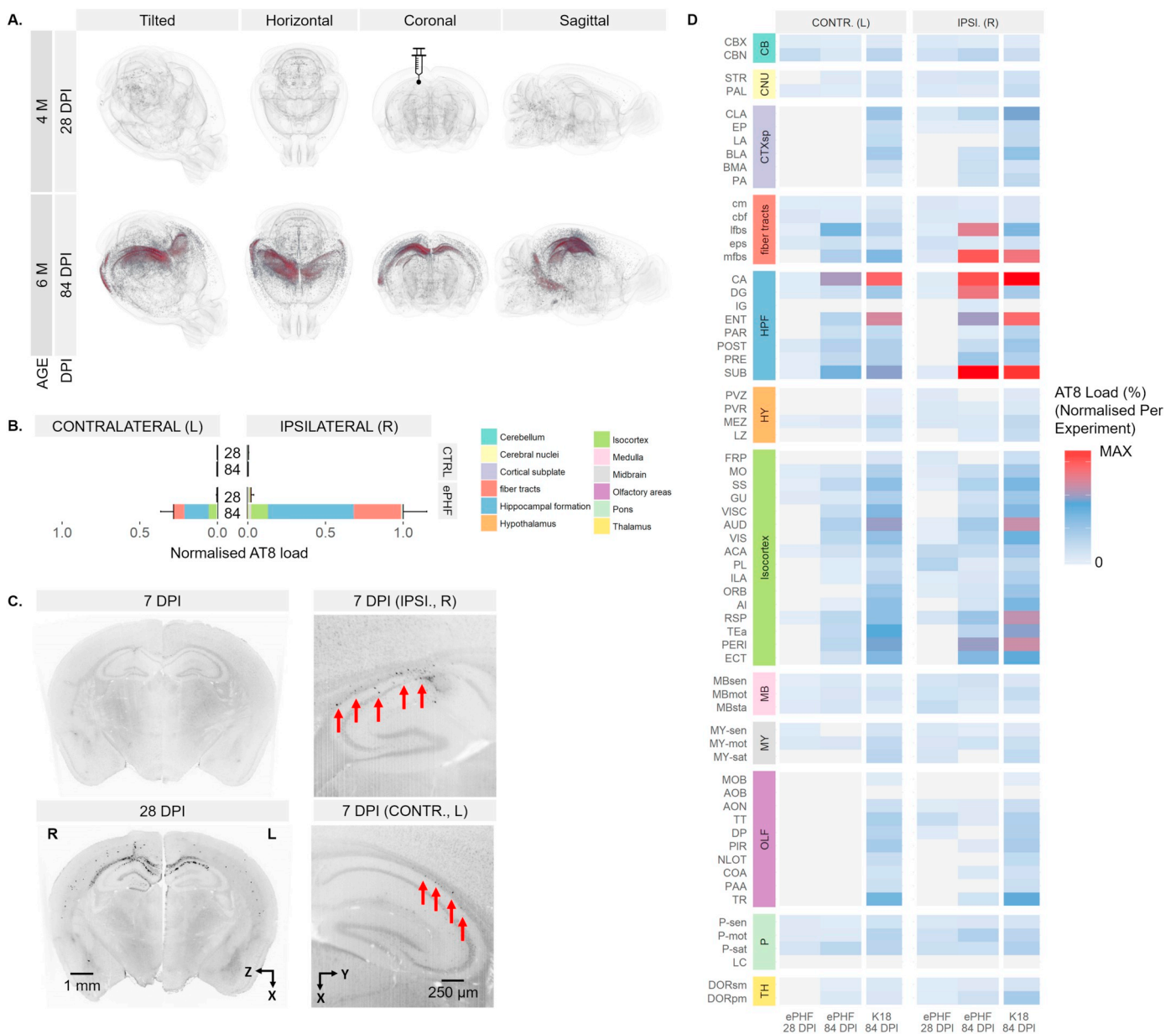
Fig. 5. ePHF injection induces similar spreading patterns as K18. A. 3D renders of average AT8 load in ePHF-injected Tau.P301L mouse brains as a function of injection time (DPI); B. Regional analysis of AT8 load over time. Bars show AT8 load (mean ± SEM) normalised to the maximum level (84 DPI, R); C. Transformed atlas of raw images shows AT8-positive staining in axonal fibre tracts at 28 DPI, and somatic staining at 84 DPI. Insets show the accumulation of AT8 signal in the fibre tracts of ispi- and contralateral alveus of the hippocampus (red arrows) on raw images; D. Sub-regional assessment of AT8 load in ePHF-injected animals, with a similar heat map of K18-injected animals at 84 DPI as a reference (gray code). The regional AT8 load was square root transformed to compress the dynamic range. No statistical analysis was performed considering the limited sample size (*n* = 3).

at this last time point were similar to those associated with K18-induced tau pathology, the kinetics differed, with AT8 signal predominantly present in axonal tracts up to 28 DPI, while somatic AT8 load emerged at 84 DPI.

3.6. Co-administration of PT83 antibody slows down tau pathology progression

To investigate if K18-induced tau pathology could be blocked, we performed K18 injection experiments in combination with a microtubule-binding domain targeting antibody (PT83). As proof of concept, we co-injected the PT83 antibody along with the K18 fibrils. We found a bilateral reduction in total AT8 load following intracerebral co-

administration (Fig. 6A, Fig. S6D). While only a limited reduction was found around the injection site, regional analysis revealed a significant decrease in most other affected brain regions (Fig. 6B). Next, we assessed whether the same antibody could reduce tau pathology development in K18 injected Tau.P301L mice upon repeated i.p. dosing. Although we found a reduction in total AT8 load as compared to controls, this difference was statistically not significant. However, regional analysis revealed a significant decrease in the contralateral hippocampal region after i.p. PT83 administration. This experiment showed that the seeding effect of K18, and the resulting accrual of hyperphosphorylated tau, can be slowed down using cerebral and, to a lesser extent, i.p. administration of a therapeutic antibody.
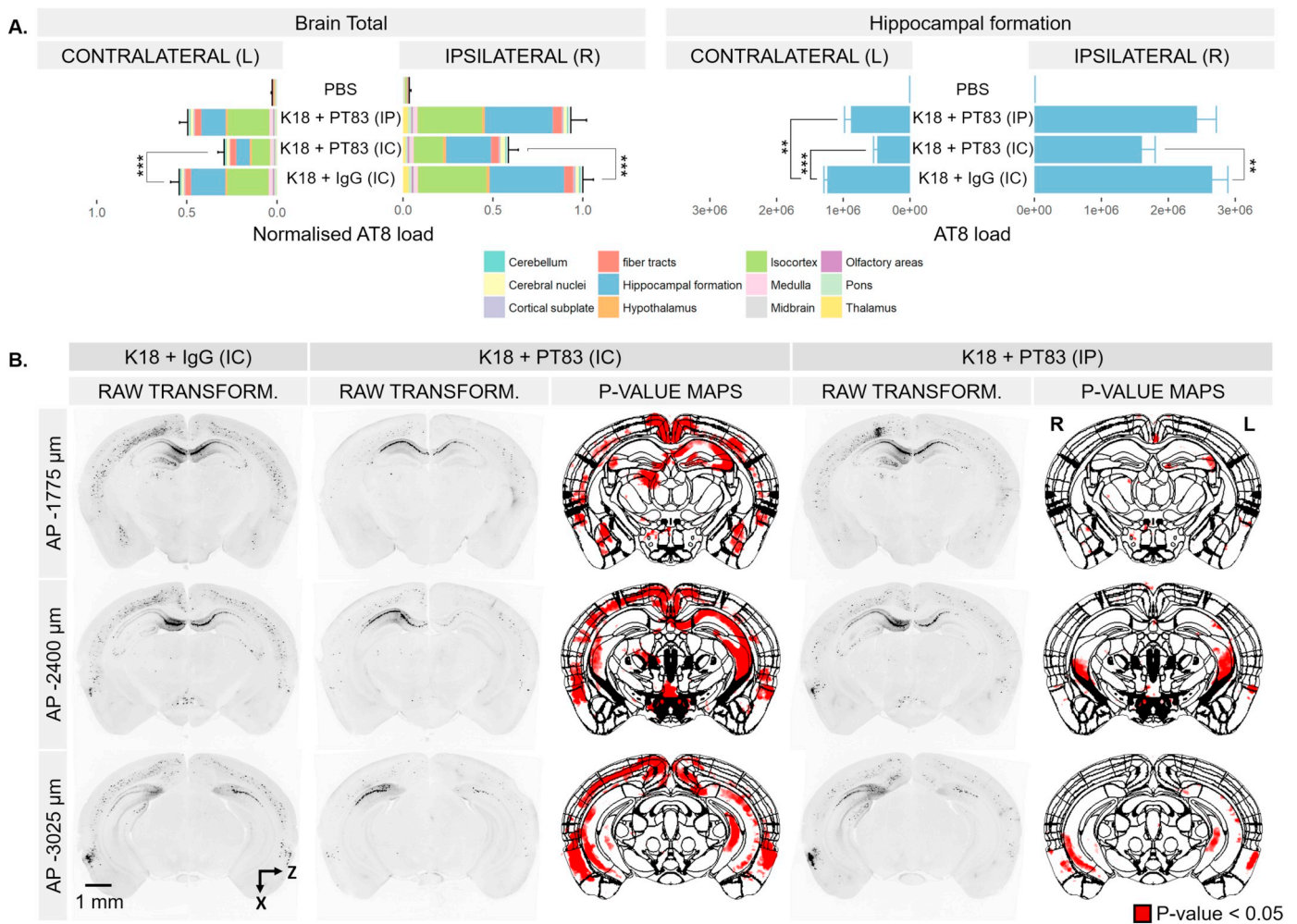
Fig. 6. PT83 administration reduces tau pathology in K18-injected animals. A. Regional AT8 load distribution in animals at 21 DPI in combination with i.c. and repeated i.p. PT83 administration. While total AT8 load was significantly decreased after i.c. administration, only the hippocampal region was significantly decreased after i.p. administration. Bars show mean ± SEM AT8 load normalised to the maximum level (K18 + IgG (IC), R); B. Atlas-transformed coronal sections of a 3D recording of representative samples of the control and treatment groups. Voxel-based analysis with *p*-value maps highlight regions that have decreased tau pathology compared to animals that received a K18 and control IgG. A representative set of biological replicates are shown in Fig. S6D. The number of biological replicates is 15, except for the PBS control (*n* = 5).

4. Discussion

To date, tissue sectioning has remained the gold standard for documenting neuropathological hallmarks in transgenic mouse brain. We have now performed a non-destructive, comprehensive staging of AT8-reactive tau pathology by exploiting tissue clearing and whole brain microscopy. Although visualisation of hyperphosphorylated tau has been achieved in cleared mouse brain before (Fu et al., 2016; Liebmann et al., 2016), we have now introduced a systematic and scalable approach for atlas-guided, regional analysis of tau pathology progression. Using this approach, we validated the age-dependent distribution pattern of tau pathology in Tau.P301L mice. Despite strong correspondence with previously documented patterns (Terwel et al., 2005), our analysis also revealed additional regions including the hypothalamus, cerebral nuclei and hippocampus. While this underlies the sensitivity of our approach, we can not establish whether the presence of AT8 signal in these regions is a result of cell autonomous development, or a result of tau spreading from previously affected regions in this model.

To study the spreading of tau pathology as observed in AD patients, we performed intracerebral injections with tau fibrils in the CA1 region of Tau.P301L mice. Although ePHF was recently demonstrated to seed hyperphosphorylated tau accrual in wild-type mice (in contrast with K18) (Guo et al., 2016), we have opted for the Tau.P301L background

to allow for a direct comparison of between both seeds. The injection was done in 3 months-old mice based on previous literature (Peeraer et al., 2015), allowing longitudinal follow-up up to 3–4 months post injection, before overt AT8 load develops as a result of the transgenic background of this model. While the concentration of injected K18 and ePHF preparations was based on previous studies (Peeraer et al., 2015; Vandermeeren et al., 2018), it should be noted that those are higher than the values of tau reported in interstitial fluid (Sato et al., 2018). Although the concentration of tau seeds in human interstitial fluid of AD patients is unknown, it might be important to take this into account as it may determine the neuronal uptake mechanism of tau (Evans et al., 2018).

The CA1 region shows abundant tau pathology in AD at an early stage (*i.e.,* Braak stage II) (Braak et al., 2006), and stereotactic injections in this region were previously validated (Peeraer et al., 2015). While it would have been relevant to target the first known region involved in AD, *i.e.,* the locus coeruleus, this is technically more challenging due to the small size of the brain nucleus (Iba et al., 2015). Moreover, targeting a structure located this deep within the brain (dorsal-ventral +3.65 mm) would also affect many more other brain sites along the injection tract, potentially decreasing the regional confinement of initial tau seeding.

In line with earlier findings with the same K18 model (Peeraer et al.,

2015), we found hyperphosphorylated tau accrual in similar regions. However, in this study, the analysis was limited to only a subset of larger, ipsilateral regions, whereas we now performed a detailed analysis of the entire brain. A section-based study in which K18 fibrils were injected in the hippocampus of Tau.P301S mice showed generally fewer affected regions (*e.g.,* contralateral cortical regions) and a slower progression (Iba et al., 2013). In contrast with this study, we found no hyperphosphorylated tau in the locus coeruleus. Moreover, the GFP pattern from the injection site did not demonstrate anatomical connections to the locus coeruleus. The latter aligns with published anatomical data of tracer experiments in the CA1 region (*e.g.,* Allen Brain Mouse Connectivity Experiment 116900714). While differences in anatomical projection data and regional tau pathology development may be attributed to the mouse strain and genetic background, it is plausibly also related to differences in the K18 fibril injection protocol (*i.e.* fibril preparation, injected volume and concentration) and the injection site, which was more ventral and posterior in the hippocampus in the cited study. Therefore, a different population of projecting neurons was targeted, and the propensity of these neurons to develop tau pathology was different between the transgenic tau mouse models in both studies. We have also targeted the entorhinal region in this study, affected earlier in AD. While quantitative differences were observed, the distribution pattern of hyperphosphorylated tau resembled that of CA1 seeding. Considering that the ENT directly projects to CA1 and both regions have shared connections to limbic and cortical structures, this finding further supports a hypothesis of tau spreading within anatomical projections in the anterograde and retrograde direction (Defelipe, 2014; Iba et al., 2015). Nevertheless, marked differences in affected brain regions between both experiments, indicate that the injection site determines tau pathology progression. The extent with which this spreading process is mediated by the intrinsic vulnerability of neurons to develop tau pathology, remains to be elucidated (Walsh and Selkoe, 2016).

Previous studies have yielded conflicting results regarding tau fibril injection induced microgliosis (Clavaguera et al., 2009; Peeraer et al., 2015). Although in our study, both K18 injection and buffer controls triggered microgliosis around the injection site, we detected a significantly higher Iba1 load in the targeted fibre tracts after K18 injection. Since the decrease in microgliosis over time did not correlate with a similar drop in hyperphosphorylated tau levels, other factors may regulate this response. These may include a decrease in the levels of other pathological tau species, a decrease in the rate of cell death and/or presence of cell debris, or a compromised microglial function as a consequence of chronic pathological conditions (Krasemann et al., 2017; Pan et al., 2011). On the other hand, we also detected a persistent subpopulation of rod-like and swollen microglia after K18 injection. This phenotype seems to be specifically associated with pathological conditions as they have been described in rat after diffuse brain injury, but also in AD patients and AD mouse models (Bachstetter et al., 2015; Chen et al., 2016; Sanders et al., 2014; Taylor et al., 2014). Microglia with swollen cell bodies are considered to be in an activated state (del Fernández-Arjona et al., 2017), which was confirmed by the presence of the activation markers CD11B and F4/80. While the function of rod-like microglia is unclear, this phenotype might mediate processes including the sealing or splinting damaged neuronal processes, or the protection of healthy neighbouring cells from injury (Taylor et al., 2014).

We demonstrated that tau pathology development after K18 injection closely matches with both the anterograde and retrograde anatomical connections of the injection site (Van Strien et al., 2009). Since it has been shown that K18 fibrils do not diffuse to remote regions, such as the contralateral hemisphere (Peeraer et al., 2015), our data suggests that the presence of hyperphosphorylated tau in connected regions is due to its intracellular spreading as opposed to a direct distal seeding effect. Furthermore, the presence of hyperphosphorylated tau outside of the connectome strengthens the hypothesis of its intercellular transmission. This is corroborated by other studies demonstrating

bidirectional propagation of tau pathology after locus coeruleus injection, followed by spreading to secondary connected regions (Iba et al., 2015). While several mechanisms for the induction and the intercellular spreading of hyperphosphorylated tau have been put forward, regional vulnerability seems to vary for distinct pathological tau strains (Guo and Lee, 2014; Kaufman et al., 2016). However, despite different spreading kinetics between K18 and ePHF seeding, the spatial spreading patterns were similar, suggesting common seeding properties for these fibril preparations.

Although tau is an intracellular protein and therefore not an evident immunization target, several active and passive immunization studies in tauopathy mice previously showed an effective decrease in pathological tau load and associated functional deficits (Congdon and Sigurdsson, 2018). We have shown that the seeding activity of K18 can be inhibited by co-injection, and to a lesser extent by repeated i.p. dosing, of PT83. Considering PT83 binds microtubule-binding domain of tau (Vandermeeren et al., 2018), it is very likely that PT83 directly inhibits K18 seeding. Although this domain normally functions to stabilise microtubules (Guo et al., 2017), it also contains aggregation-prone residues and is responsible for pathological tau interactions (Fitzpatrick et al., 2017; Kontsekova et al., 2014; Mukrasch et al., 2009). Only a single other study demonstrated this effect in a K18-seeded mouse model to date using PHF13 (Sankaranarayanan et al., 2015). This antibody targets pS396 in the c-terminus region of tau, *i.e.,* outside the K18 region, and is considered to operate by binding brain-derived tau. Further studies that directly compare both antibodies, including similar seeding and antibody dosing schemes would be valuable to identify the most effective epitope to inhibit tau pathology development. Exactly how passive immunization reduces tau pathology is poorly understood, but it may be the result of extracellular clearance of tau *via* glial activation, intracellular degradation, or by inhibiting tau interactions thus preventing the seeding effect (Congdon et al., 2013; Ising et al., 2017; Luo et al., 2015). The ostensible lack of decrease in AT8 load at the injection site may indicate that the K18-induced tau pathology is locally saturated, and that the local K18 concentration is too high for PT83 to block all K18-tau interaction. The limited reduction in total AT8 load found after repeated i.p. dosing is likely a result of the limited penetration of PT83 through the tightly regulated blood-brain-barrier (BBB) (Paul, 2011). However, we could detect a significant decrease in the contralateral hippocampal AT8 load after i.p. dosing, indicating that regional assessment allows more sensitive evaluation of therapeutics. Nevertheless, more effective therapeutic delivery strategies are needed. Increased bioavailability might be achieved with small antibody fragments (Krishnaswamy et al., 2014), by exploiting BBB shuttle mechanisms (Hultqvist et al., 2017), or by temporary BBB disruption using high-intensity focused ultrasound or by co-administration with vasoactive or osmotic substances (Marcos-Contreras et al., 2016; McDannold et al., 2008). Although K18 fragments only represent a truncated version of tau protein, this result shows that K18 can be targeted by passive immunization. However, follow-up studies with ePHFs are necessary to demonstrate the translational value of this approach. Moreover, it would of interest to assess whether the demonstrated therapeutic effect of PT83 may also have protective effects on downstream effects of K18, such as glial activation. In conclusion, the combination of injection experiments with whole-brain microscopy offers a novel approach to assess the spatiotemporal dynamics of different tau strains and measure the effects of therapeutic interventions aiming at slowing down or halting the progression of tau pathology.

Supplementary data to this article can be found online at https://doi.org/10.1016/j.nbd.2019.03.010.

Declaration of interests

References

Allen, B., Ingram, E., Takao, M., Smith, M.J., Jakes, R., Virdee, K., Yoshida, H., Holzer, M., Craxton, M., Emson, P.C., et al., 2002. Abundant tau filaments and nonapoptotic neurodegeneration in transgenic mice expressing human P301S tau protein. J. Neurosci. 22, 9340–9351.

Åslund, A., Sigurdson, C.J., Klingstedt, T., Grathwohl, S., Bolmont, T., Dickstein, D.L., Glimsdal, E., Prokop, S., Lindgren, M., Konradsson, P., et al., 2009. Novel pentameric thiophene derivatives for in vitro and in vivo optical imaging of a plethora of protein aggregates in cerebral amyloidoses. ACS Chem. Biol. 4, 673–684.

Bachstetter, A.D., Van Eldik, L.J., Schmitt, F.A., Neltner, J.H., Ighodaro, E.T., Webster, S.J., Patel, E., Abner, E.L., Kryscio, R.J., Nelson, P.T., 2015. Disease-related microglia heterogeneity in the hippocampus of Alzheimer's disease, dementia with Lewy bodies, and hippocampal sclerosis of aging. Acta Neuropathol. Commun. 3, 32.

Barbier, M., Bottelbergs, A., Nuydens, R., Ebneth, A., De Vos, W.H., 2017. SliceMap: an algorithm for automated brain region annotation. Bioinformatics 34, 718–720.

Benjamini, Y., Hochberg, Y., 1995. Controlling the false discovery rate: a practical and powerful approach to multiple testing. J. R. Stat. Soc. 57, 289–300.

Braak, H., Braak, E., 1991. Neuropathological staging of Alzheimer-related changes. Acta Neuropathol. 239–259.

Braak, H., Del Tredici, K., 2004. Alzheimer's disease: Intraneuronal alterations precede insoluble amyloid-β formation. Neurobiol. Aging 25, 713–718.

Braak, H., Alafuzoff, I., Arzberger, T., Kretzschmar, H., Del Tredici, K., 2006. Staging of Alzheimer disease-associated neurofibrillary pathology using paraffin sections and immunocytochemistry. Acta Neuropathol. 112, 389–404.

Brettschneider, J., Del Tredici, K., Lee, V.M.Y., Trojanowski, J.Q., 2015. Spreading of pathology in neurodegenerative diseases: a focus on human studies. Nat. Rev. Neurosci. 16, 109–120.

Brier, M.R., Gordon, B., Friedrichsen, K., McCarthy, J., Stern, A., Christensen, J., Owen, C., Aldea, P., Su, Y., Hassenstab, J., et al., 2016. Tau and ab imaging, CSF measures, and cognition in Alzheimer's disease. Sci. Transl. Med. 8, 1–10.

Chen, W., Abud, E.A., Yeung, S.T., Lakatos, A., Nassi, T., Wang, J., Blum, D., Buée, L., Poon, W.W., Blurton-Jones, M., 2016. Increased tauopathy drives microglia-mediated clearance of beta-amyloid. Acta Neuropathol. Commun. 4, 63.

Chételat, G., La Joie, R., Villain, N., Perrotin, A., De La Sayette, V., Eustache, F., Vandenberghe, R., 2013. Amyloid imaging in cognitively normal individuals, at-risk populations and preclinical Alzheimer's disease. NeuroImage Clin. 2, 356–365.

Cho, H., Choi, J.Y., Hwang, M.S.B.S.N., Lee, J.H., Kim, Y.J., Lee, H.M., Lyoo, C.H., Ryu, Y.H., Lee, M.S., 2016. Tau PET in Alzheimer disease and mild cognitive impairment. Neurology 87, 375–383.

Clavaguera, F., Bolmont, T., Crowther, R.A., Abramowski, D., Frank, S., Probst, A., Fraser, G., Stalder, A.K., Beibel, M., Staufenbiel, M., et al., 2009. Transmission and spreading of tauopathy in transgenic mouse brain. Nat. Cell Biol. 11, 909–913.

Congdon, E.E., Sigurdsson, E.M., 2018. Tau-targeting therapies for Alzheimer disease. Nat. Rev. Neurol. 14, 399–415.

Congdon, E.E., Gu, J., Sait, H.B.R., Sigurdsson, E.M., 2013. Antibody uptake into neurons occurs primarily via clathrin-dependent Fc receptor endocytosis and is a prerequisite for acute tau protein clearance. J. Biol. Chem. 288, 35452–35465.

De Calignon, A., Polydoro, M., Suárez-Calvet, M., William, C., Adamowicz, D.H., Kopeikina, K.J., Pitstick, R., Sahara, N., Ashe, K.H., Carlson, G.A., et al., 2012.

Propagation of tau pathology in a model of early Alzheimer's disease. Neuron 73, 685–697.

Defelipe, J., 2014. Selective Alterations of Neurons and Circuits Related to Early Memory Loss in Selective Alterations of Neurons and Circuits Related to Early Memory Loss in Alzheimer's Disease.

del Fernández-Arjona, M., Grondona, J.M., Fernández-Llebrez, P., Granados-Durán, P., López-Ávalos, M.D., 2017. Microglia morphological categorization in a rat model of neuroinflammation by hierarchical cluster and principal components analysis. Front. Cell. Neurosci. 11, 1–22.

Evans, L.D., Wassmer, T., Fraser, G., Smith, J., Perkinton, M., Billinton, A., Livesey, F.J., 2018. Extracellular monomeric and aggregated tau efficiently enter human neurons through overlapping but distinct pathways. Cell Rep. 22, 3612–3624.

Fitzpatrick, A.W.P., Falcon, B., He, S., Murzin, A.G., Murshudov, G., Garringer, H.J., Crowther, R.A., Ghetti, B., Goedert, M., Scheres, S.H.W., 2017. Cryo-EM structures of tau filaments from Alzheimer's disease. Nature 547, 185–190.

Fu, H., Hussaini, S.A., Wegmann, S., Profaci, C., Daniels, J.D., Herman, M., Emrani, S., Figueroa, H.Y., Hyman, B.T., Davies, P., et al., 2016. 3D visualization of the temporal and spatial spread of tau pathology reveals extensive sites of tau accumulation associated with neuronal loss and recognition memory deficit in aged tau transgenic mice. PLoS One 11, 1–20.

Greenberg, S.G., Davies, P., 1990. A preparation of Alzheimer paired helical filaments that displays distinct tau proteins by polyacrylamide gel electrophoresis. Proc. Natl. Acad. Sci. U. S. A. 87, 5827–5831.

Guo, J.L., Lee, V.M.Y., 2014. Cell-to-cell transmission of pathogenic proteins in neurodegenerative diseases. Nat. Med. 20, 130–138.

Guo, J.L., Narasimhan, S., Changolkar, L., He, Z., Stieber, A., Zhang, B., Gathagan, R.J., Iba, M., McBride, J.D., Trojanowski, J.Q., et al., 2016. Unique pathological tau conformers from Alzheimer's brains transmit tau pathology in nontransgenic mice. J. Exp. Med. 213, 2635–2654.

Guo, T., Noble, W., Hanger, D.P., 2017. Roles of tau protein in health and disease. Acta Neuropathol. 133, 665–704.

Holmes, B.B., Furman, J.L., Mahan, T.E., Yamasaki, T.R., Mirbaha, H., Eades, W.C., Belaygorod, L., Cairns, N.J., Holtzman, D.M., Diamond, M.I., 2014. Proteopathic tau seeding predicts tauopathy in vivo. Proc. Natl. Acad. Sci. U. S. A. 111, 85.

Hultqvist, G., Syvänen, S., Fang, X.T., Lannfelt, L., Sehlin, D., 2017. Bivalent brain shuttle increases antibody uptake by monovalent binding to the transferrin receptor. Theranostics 7, 308–318.

Iba, M., Guo, J.L., McBride, J.D., Zhang, B., Trojanowski, J.Q., Lee, V.M.-Y., 2013. Synthetic tau fibrils mediate transmission of neurofibrillary tangles in a transgenic mouse model of Alzheimer's-like tauopathy. J. Neurosci. 33, 1024–1037.

Iba, M., McBride, J.D., Guo, J.L., Zhang, B., Trojanowski, J.Q., Lee, V.M.Y., 2015. Tau pathology spread in PS19 tau transgenic mice following locus coeruleus (LC) injections of synthetic tau fibrils is determined by the LC's afferent and efferent connections. Acta Neuropathol. 130, 349–362.

Ising, C., Gallardo, G., Leyns, C.E.G., Wong, C.H., Jiang, H., Stewart, F., Koscal, L.J., Roh, J., Robinson, G.O., Remolina Serrano, J., et al., 2017. AAV-mediated expression of anti-tau scFvs decreases tau accumulation in a mouse model of tauopathy. J. Exp. Med. 214, 1227–1238.

Kaufman, S.K., Sanders, D.W., Thomas, T.L., Ruchinskas, A.J., Vaquer-Alicea, J., Sharma, A.M., Miller, T.M., Diamond, M.I., 2016. Tau prion strains dictate patterns of cell pathology, progression rate, and regional vulnerability in vivo. Neuron 92, 796–812.

Kilkenny, C., Browne, W.J., Cuthill, I.C., Emerson, M., Altman, D.G., 2013. Improving bioscience research reporting: the arrive guidelines for reporting animal research. Animals 4, 35–44.

Kim, Y., Venkataraju, K.U., Pradhan, K., Mende, C., Taranda, J., Turaga, S.C., Arganda-Carreras, I., Ng, L., Hawrylycz, M.J., Rockland, K.S., et al., 2015. Mapping social behavior-induced brain activation at cellular resolution in the mouse. Cell Rep. 10, 292–305.

Klein, S., Staring, M., Murphy, K., Viergever, M.A., Pluim, J.P.W., 2010. Elastix: a toolbox for intensity-based medical image registration. IEEE Trans. Med. Imaging 29, 196–205.

Kontsekova, E., Zilka, N., Kovacech, B., Skrabana, R., Novak, M., 2014. Identification of structural determinants on tau protein essential for its pathological function: novel therapeutic target for tau immunotherapy in Alzheimer's disease. Alzheimers Res. Ther. 6, 45.

Krasemann, S., Madore, C., Cialic, R., Baufeld, C., Calcagno, N., El Fatimy, R., Beckers, L., O'Loughlin, E., Xu, Y., Fanek, Z., et al., 2017. The TREM2-APOE pathway drives the transcriptional phenotype of dysfunctional microglia in neurodegenerative diseases. Immunity 47, 566–581 (e9).

Krishnaswamy, S., Lin, Y., Rajamohamedsait, W.J., Rajamohamedsait, H.B., Krishnamurthy, P., Sigurdsson, E.M., 2014. Antibody-derived in vivo imaging of tau pathology. J. Neurosci. 34, 16835–16850.

Liebmann, T., Renier, N., Bettayeb, K., Greengard, P., Tessier-Lavigne, M., Flajolet, M., 2016. Three-dimensional study of Alzheimer's disease hallmarks using the iDISCO clearing method. Cell Rep. 16, 1138–1152.

Luo, W., Liu, W., Hu, X., Hanna, M., Caravaca, A., Paul, S.M., 2015. Microglial internalization and degradation of pathological tau is enhanced by an anti-tau monoclonal antibody. Sci. Rep. 5, 1–12.

Malia, T.J., Teplyakov, A., Ernst, R., Wu, S.J., Lacy, E.R., Liu, X., Vandermeeren, M., Mercken, M., Luo, J., Sweet, R.W., et al., 2016. Epitope mapping and structural basis for the recognition of phosphorylated tau by the anti-tau antibody AT8. Proteins Struct. Funct. Bioinforma. 84, 427–434.

Marcos-Contreras, O.A., Martinez de Lizarrondo, S., Bardou, I., Orset, C., Pruvost, M., Anfray, A., Frigout, Y., Hommet, Y., Lebouvier, L., Montaner, J., et al., 2016. Hyperfibrinolysis increases blood-brain barrier permeability by a plasmin- and bradykinin-dependent mechanism. Blood 128, 2423–2434.

Masters, C.L., Bateman, R., Blennow, K., Rowe, C.C., Sperling, R.A., Cummings, J.L., 2015. Alzheimer's disease. Nat. Rev. Dis. Prim. 1, 1–18.

McDannold, N., Vykhodtseva, N., Hynynen, K., 2008. Blood-brain barrier disruption induced by focused ultrasound and circulating preformed microbubbles appears to be characterized by the mechanical index. Ultrasound Med. Biol. 34, 834–840.

Meyer-Spradow, J., Ropinski, T., Mensmann, J., Hinrichs, K., 2009. Voreen: a rapid-prototyping environment for ray-casting-based volume visualizations. IEEE Comput. Graph. Appl. 29, 6–13.

Mukrasch, M.D., Bibow, S., Korukottu, J., Jeganathan, S., Biernat, J., Griesinger, C., Mandelkow, E., Zweckstetter, M., 2009. Structural polymorphism of 441-residue tau at single residue resolution. PLoS Biol. 7, 0399–0414.

Oddo, S., Caccamo, A., Shepherd, J.D., Murphy, M.P., Golde, T.E., Kayed, R., Metherate, R., Mattson, M.P., Akbari, Y., LaFerla, F.M., 2003. Triple-transgenic model of Alzheimer's disease with plaques and TanglesIntracellular Aβ and synaptic dysfunction. Neuron 39, 409–421.

Pan, X.D., Zhu, Y.G., Lin, N., Zhang, J., Ye, Q.Y., Huang, H.P., Chen, X.C., 2011. Microglial phagocytosis induced by fibrillar β-amyloid is attenuated by oligomeric β-amyloid: implications for Alzheimer's disease. Mol. Neurodegener. 6 (1), 45.

Pan, C., Cai, R., Quacquarelli, F.P., Ghasemigharagoz, A., Lourbopoulos, A., Matryba, P., Plesnila, N., Dichgans, M., Hellal, F., Ertürk, A., 2012. Shrinkage-mediated imaging of entire organs and organisms using uDISCO. Nat. Methods 13 (10), 859–867.

Paul, S.M., 2011. Therapeutic antibodies for brain disorders. Sci. Transl. Med. 3 (84ps20-84ps20).

Peeraer, E., Bottelbergs, A., Van Kolen, K., Stancu, I.-C., Vasconcelos, B., Mahieu, M., Duytschaever, H., Ver Donck, L., Torremans, A., Sluydts, E., et al., 2015. Intracerebral injection of preformed synthetic tau fibrils initiates widespread tauopathy and neuronal loss in the brains of tau transgenic mice. Neurobiol. Dis. 73, 83–95.

Perea, J.R., Llorens-Martín, M., Ávila, J., Bolós, M., 2018. The role of microglia in the spread of tau: relevance for tauopathies. Front. Cell. Neurosci. 12, 1–8.

Preibisch, S., Saalfeld, S., Tomancak, P., 2009. Globally optimal stitching of tiled 3D microscopic image acquisitions. Bioinformatics 25, 1463–1465.

Renier, N., Adams, E.L., Kirst, C., Wu, Z., Azevedo, R., Kohl, J., Autry, A.E., Kadiri, L., Umadevi Venkataraju, K., Zhou, Y., et al., 2016. Mapping of brain activity by automated volume analysis of immediate early genes. Cell 165, 1789–1802.

Richardson, D.S., Lichtman, J.W., 2015. Clarifying tissue clearing. Cell 162, 246–257.

Sanders, D.W., Kaufman, S.K., DeVos, S.L., Sharma, A.M., Mirbaha, H., Li, A., Barker, S.J., Foley, A.C., Thorpe, J.R., Serpell, L.C., et al., 2014. Distinct tau prion strains propagate in cells and mice and define different tauopathies. Neuron 82, 1271–1288.

Sankaranarayanan, S., Barten, D.M., Vana, L., Devidze, N., Yang, L., Cadelina, G., Hoque, N., DeCarr, L., Keenan, S., Lin, A., et al., 2015. Passive immunization with phospho-tau antibodies reduces tau pathology and functional deficits in two distinct mouse tauopathy models. PLoS One 10, 1–28.

Sato, C., Barthélemy, N.R., Mawuenyega, K.G., Patterson, B.W., Gordon, B.A., Jockel-Balsarotti, J., Sullivan, M., Crisp, M.J., Kasten, T., Kirmess, K.M., et al., 2018. Tau kinetics in neurons and the human central nervous system. Neuron 97, 1284–1298 (e7).

Spires-Jones, T.L., Hyman, B.T., 2014. The intersection of amyloid beta and tau at synapses in Alzheimer's disease. Neuron 82, 756–771.

Taylor, S.E., Morganti-Kossmann, C., Lifshitz, J., Ziebell, J.M., 2014. Rod microglia: a morphological definition. PLoS One 9.

Terwel, D., Lasrado, R., Snauwaert, J., Vandeweert, E., Van Haesendonck, C., Borghgraef, P., Van Leuven, F., 2005. Changed conformation of mutant tau-P301L underlies the moribund tauopathy, absent in progressive, nonlethal axonopathy of tau-4R/2N transgenic mice. J. Biol. Chem. 280, 3963–3973.

Van Strien, N.M., Cappaert, N.L.M., Witter, M.P., 2009. The anatomy of memory: an interactive overview of the parahippocampal- hippocampal network. Nat. Rev. Neurosci. 10, 272–282.

Vandermeeren, M., Borgers, M., Van Kolen, K., Theunis, C., Vasconcelos, B., Bottelbergs, A., Wintmolders, C., Daneels, G., Willems, R., Dockx, K., et al., 2018. Anti-tau monoclonal antibodies derived from soluble and filamentous tau show diverse functional properties in vitro and in vivo. J. Alzheimers Dis. 65, 265–281.

Walsh, D.M., Selkoe, D.J., 2016. A critical appraisal of the pathogenic protein spread hypothesis of neurodegeneration. Nat. Rev. Neurosci. 17, 251–260.

Zheng-Fischhöfer, Q., Biernat, J., Mandelkow, E.M., Illenberger, S., Godemann, R., Mandelkow, E., 1998. Sequential phosphorylation of Tau by glycogen synthase kinase-3β and protein kinase a at Thr212 and Ser214 generates the Alzheimer-specific epitope of antibody AT100 and requires a paired-helical-filament-like conformation. Eur. J. Biochem. 252, 542–552.